CERN – EUROPEAN ORGANIZATION FOR NUCLEAR RESEARCH

THE TRANSVERSE AND LONGITUDINAL BEAM CHARACTERISTICS OF THE PHIN PHOTO-INJECTOR AT CERN

Ö. Mete [1][2], E. Chevallay[1], A. Dabrowski[1], M. Divall[1], S. Döbert[1], D. Egger[1][2], K. Elsener[1], V. Fedosseev[1], T. Lefèvre[1], M. Petrarca[1]

[1] CERN, Geneva, Switzerland; [2] EPFL, Lausanne

Abstract

A new photo-injector, capable to deliver a long pulse train with a high charge per bunch for CTF3, has been designed and installed by a collaboration between LAL, CCLRC and CERN within the framework of the second Joint Research Activity PHIN of the European CARE program. The demonstration of the high charge and the stability along the pulse train are the important goals for CTF3 and the CLIC drive beam. The nominal beam for CTF3 has an average current of 3.5 A, a 1.5 GHz bunch repetition frequency and a pulse length of 1.27 μs (1908 bunches). The existing CTF3 injector consists of a thermionic gun and a subharmonic bunching system. The PHIN photo-injector is being tested in a dedicated test-stand at CERN to replace the existing CTF3 injector that is producing unwanted satellite bunches during the bunching process. A phase-coding scheme is planned to be implemented to the PHIN laser system providing the required beam temporal structure by CTF3. RF photo-injectors are high-brightness, low-emittance electron sources. One of the main beam dynamics issues for a high brightness electron source, is the optimization of beam envelope behavior in the presence of the space charge force in order to control the beam emittance. Beam based measurements, such as single shot emittance measurement with a multi-slit configuration, have been performed during the commissioning runs in 2008 and 2009. In this work the photo-injector will be described and the first beam test results will be presented and compared with simulations.

Geneva, Switzerland
22/03/2010

Contents

List of Figures

List of Tables

1 INTRODUCTION

A photo-injector was proposed as an option for Compact Linear Collider (CLIC) Test Facility 3 (CTF3) and later for the CLIC drive beam [1, 2, 3, 4]. The PHIN photo-injector has been installed in a dedicated test-stand at CERN. The beam measurements have been done in a wide range of parameter settings such as focusing, laser spot size and pulse length, charge per bunch and energy, in order to characterize the longitudinal and the transverse properties. In RF photo-injectors, the transverse phase-space dynamics are influenced by several issues such as the time dependency of the RF field, space charge effects [5] and transverse focusing. The space charge effect can be compensated with the field created by a focusing solenoid [6]. The adjustment of the laser properties such as spot size, radial and temporal distribution can be used to control the initial properties of the beam. During the high charge operation at low energies, the space charge force is the dominating effect for emittance growth. The laser spot size dependence of the transverse size and emittance of the beam has been investigated for 2, 3 and 4 mm laser spots. The transverse emittance was measured with the multi-slit method in a range of focusing solenoid currents to study the emittance compensation.

2 SET-UP

The beamline consists of three sections, cathode transfer chamber, RF gun and the beam measurements section (Figure 1).
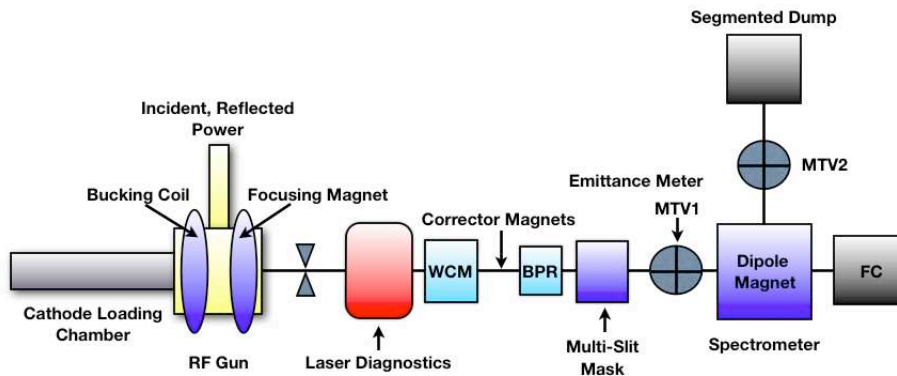

Figure 1: The PHIN photo-injector layout.

2.1 Cathode Transfer Chamber (Cathode Carrier)

The electrons are extracted from a semiconductor Cs_2Te cathode, which is mounted on one end of a 2+1/2 cell RF gun. The cathode has been developed by the CERN photo-emission laboratory and demonstrated a lifetime to allow >100h run at a 3% quantum efficiency for a 262 nm laser wavelength [7]. Excellent vacuum conditions, $P <= 10^{-11}$ mbar, and bakeout at 300°C are mandatory to achieve this quantum lifetime.

The cathode transfer chamber, the so-called "Transport Carrier" (or T.C.), is a mechanical device designed to receive and deliver up to four photocathodes, under Ultra High Vacuum conditions (U.H.V.), from the photo-emission laboratory to the PHIN photo-injector.

Before the measurements at the PHIN set-up, a bakeout at 130°C has been done. The vacuum values of ~ 3 x 10^{-10} and $\sim 10^{-9}$ mbar have been reached without and with the RF and the beam, respectively.

2.2 Laser

A Nd:YLF oscillator produces vertically polarized pulses at a repetition rate of 1.5 GHz with an average power of P~300mW. The central wavelength is 1047 nm and the pulse width is ~8 ps (FWHM). After the pre-amplification and two additional amplification stages from 300 mW to 9 kW, the length of the pulse train is adjusted using the Pockels cells between 1 ns and tens of μs [8, 9, 10]. The nominal pulse train length is 1.27 μs, at 1-50 Hz pulse repetition rate and 1.5 GHz bunch repetition rate, according to the PHIN design specifications. After the UV conversion [11], the train of 1908 pulses with the energy of 370 nJ/pulse is obtained on the photocathode. This is the nominal energy in order to extract the bunch charge of 2.33 nC assuming the quantum efficiency of 3% [12]. The laser spot size on the photocathode can be changed within a range of 0.1-5 mm (4σ). During the commissioning runs a laser with the pulse train length of 200 ns was generally used, obtaining 300 bunches. The laser spot sizes of 2, 3, 4 mm have been used for different measurements that will be explained later in the text. An additional beam size measurement has also been done by using a 1.2 μs pulse train. The layout of the laser is shown in Figure 2 .
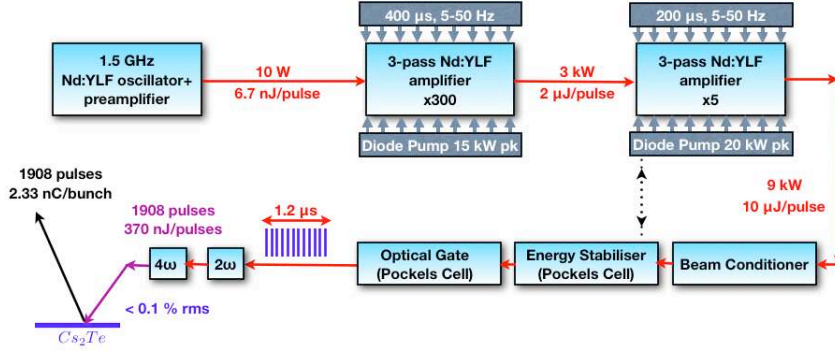
Figure 2: Layout of the laser system.

Table 1: Specifications for CTF3 photo-injector.

Parameter	Value
RF Frequency (GHz)	2.99855
RF Power (MW)	30
Beam Energy (MeV)	5.5
Beam Current (A)	3.51
Charge / Bunch (nC)	2.33
Bunch Length (ps)	10
Energy Spread (%)	<2
Normalized Emittance (mm mrad)	<25
Pulse Train Duration (μs)	1.27
Vacuum Pressure (mbar)	2.10^{-10}

2.3 RF Gun

A $2+1/2$ RF gun, that was designed by LAL, has been installed in the set-up. The design has been based on a previous proto-type CERN RF gun and has been modified in order to provide the specifications defined for the CTF3 photo-injector, seen in the Table.1. It has been optimised for the high charge by choosing an angle to the half-cell wall, around the photo-cathode, to provide additional transverse focusing. This angle was reduced from the previous value of $8°$ to $3.4°$. Additionally, the shape of the iris was changed from circular to elliptical to decrease the surface electric field and therefore minimize the electrical breakdown and dark current levels. The details can be found in reference [13].

2.4 Measurement Section

A focusing solenoid follows after the gun as a transverse focusing element that ensures the emittance compensation. The so called "bucking coil" was installed around the cathode. This maintains zero magnetic field on the cathode surface, preventing the emittance growth caused by the residual cathode field [14]. The laser diagnostics was placed close to the gun providing the alignment of the laser on the cathode after the laser table. The third section of the beamline consists of several diagnostics tools where a wall current monitor (WCM) and a beam position RF monitor (BPR) have also been included. A set of corrector magnets have been installed for horizontal and vertical corrections in addition to the focusing solenoid. For the emittance measurements a 2 mm thick tungsten multi-slit mask was utilized. The mask has 25 slits with a width of 100 μm, spaced by 900 μm. A 25 μm thick aluminum OTR (Optical Transition Radiation) screen, at $45°$ incidence to the beam, was used in the system to image the beamlets after the slits. A Faraday cup was placed after the emittance-meter for charge measurements. The energy spread measurement has been done with a spectrometer, installed at the end of the beamline. The spectrometer consists of a dipole magnet placed before the Faraday cup, a ceramic screen and a CCD camera. The beam is transported to the spectrometer line instead of being dumped in the Faraday cup when the dipole is active.

The PHIN set-up has been tested for the first time in November 2008 [15]. In the second PHIN run (March 2009), the CCD camera in the emittance-meter has been replaced by an intensified, gated, CCD camera allowing the use of an aluminum OTR screen. It has been chosen as a better solution than a ceramic screen that is more sensitive than the aluminum one but often saturates with the usual operation electron intensity[1]. Furthermore, the response of the OTR screen is faster than the ceramic screen, and hence when coupled to the gated camera, OTR screen can be used for "time resolved" profile measurements. A segmented dump has been installed at the end of the spectrometer line and tested in the second PHIN run allowing the measurement of the time resolved

---

[1]The aluminum screen has been used during the March 2009 run. It has been replaced with a SiC screen and a new non-reflective screen holder has been utilized in September 2009.

Table 2: Some of the parameters used in the PARMELA simulations.

Parameter	I	II	III
RF Frequency (GHz)	2.99855		
Gradient (MV/m)	88	85.4	80.6
Phase* (°)	35		
Laser Spot Size** (mm)	0.8	1.2	1.6
Beam Energy (MeV)	5.7	5.2	5.5
Charge/Bunch (nC)	1.28	1.28	1.09

Arbitrary phase of the RF cavity with respect to the start time of the simulations, to obtain the optimized beam parameters.
**Laser spot size has been given as the 1σ.*

longitudinal beam properties. And the existing spectrometer has been upgraded by replacing the ceramic screen and the CCD with an aluminum foil and an intensified, gated, CCD camera.

3 MEASUREMENTS

3.1 Beam Size Measurements

The electron beam size was measured and compared with the PARMELA [16] simulations. In PARMELA simulations, the initial parameters of an electron beam emerging from a photocathode are given by the laser properties. These initial properties of the beam develop during the simulation according to the beamline elements. Therefore the electron beam was defined as a round beam with a Gaussian distribution, having a 8 ps bunch length, in the simulations. Some of the parameters used as the PARMELA input are shown in Table 2.
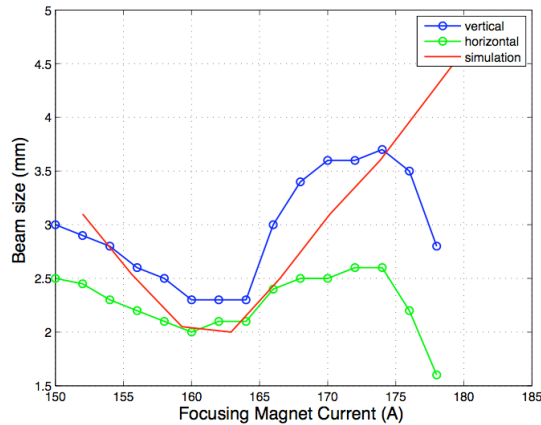

Figure 3: The beam size scan during the November 2008 run.

As the result of the first run, an asymmetric behavior has been observed between the vertical and horizontal beam size (Figure 3). The optics for the laser alignment and the positioning on the cathode, and the background field by the magnetic components in the set-up have been considered as the possible sources to be investigated for the asymmetry. Upon these investigations, it turned out that the laser was not centered on the cathode, along the axis of the RF gun. This has been corrected by re-alignment of the laser in the region. During the second commissioning run in March 2009, the asymmetry in the beam envelope for the vertical and the horizontal beam sizes was no longer present, confirming a laser alignment problem before the re-alignment.

Beam size scans have been performed with respect to different laser spot sizes of 2, 3, and 4 mm at 5.7, 5.2 and 5.5 MeV, respectively. The laser spot size is given as knife edge value, defined as the spot size regarding 85% of the profile. The corresponding 1σ (64%) values of the laser spot sizes are 0.8 mm, 1.2 mm and 1.6 mm and these values have been used in the PARMELA simulations. The results of the beam size scans are shown in Figure 4 and compared with the PARMELA simulations. The simulations and the measurements agree rather well with the exception of the focus region. This region is the optical focus of the beam, where the beam waist occurs. The investigation on the 3D intensity distributions showed that, the discrepancy is due to the saturation of the intensified CCD camera (Figure 5). In order to reconstruct the intensity distribution by taking into account the saturation effect, the cross sections of the 3D profiles have been studied for the complete beam size scan for 2 mm laser spot size. The reconstruction of a single measured point and the result of the reconstruction for the complete scan were demonstrated, (Figure 6) showing the agreement of data and simulation at the focus region. During the scans the beam size has been measured several times at one particular focusing solenoid current setting. These subsequent measurements in the same setting have been used to calculate the statistical
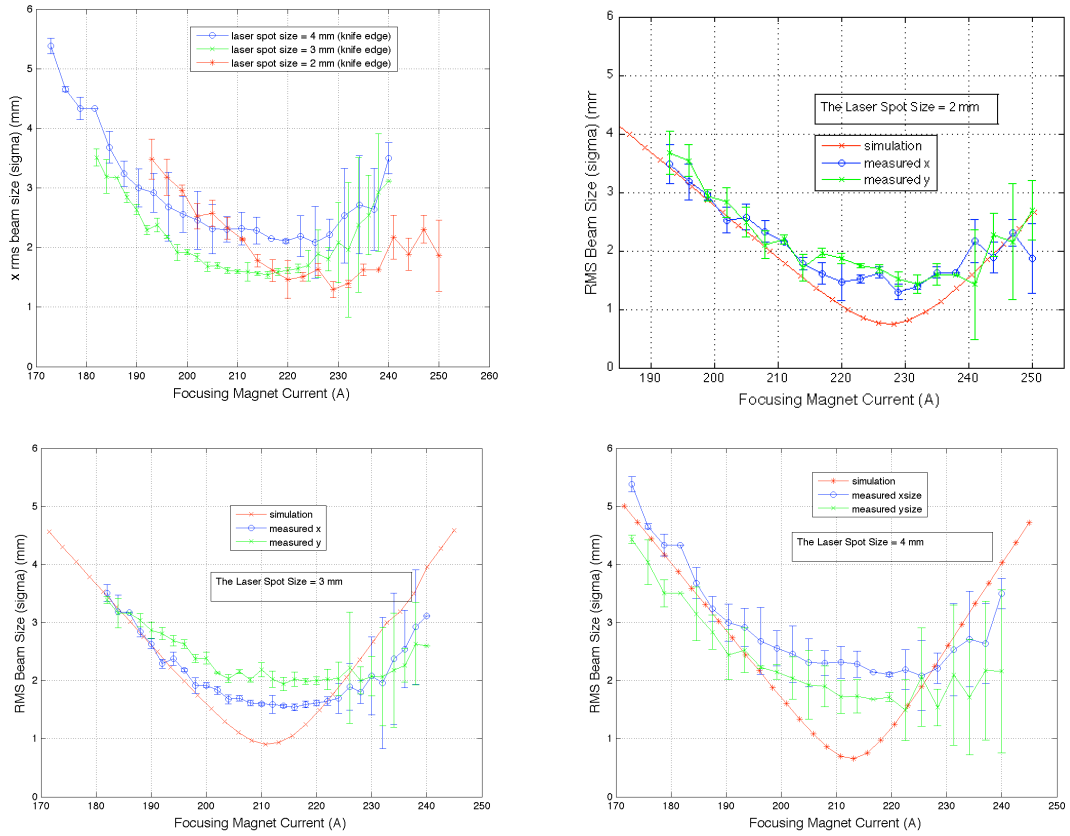
Figure 4: Focusing solenoid scans for the transverse beam size measurement for different laser spot sizes.
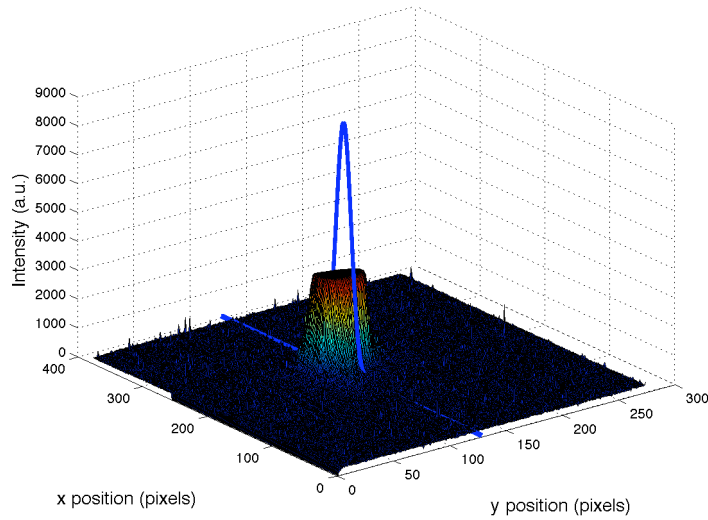
Figure 5: The intensity profile of the beam under the saturation effect of the CCD camera.

error on the corresponding measurement point. After the focus region, one observes larger measured statistical fluctuations. This could be related with the intensity fluctuations under the focusing conditions during that part of the measurement and this behavior is still under investigation. The intensity and position fluctuations during the measurements have been given in the Appendix B. Measurements showed that the minimum spot size scales with the laser spot size as expected.

Additionally, since the stability of the beam parameters along the pulse train is very important for CTF3, a 1.2 μs-long pulse train has been provided and the beam size has been measured as a function of time along the train by using a gated camera. The measurement shown on Figure 7 has been done by capturing the beam profile images with a constant camera gate of 100 ns. Each time the camera gate delay increased with the steps of 100 ns to observe a different longitudinal position along the pulse train. The

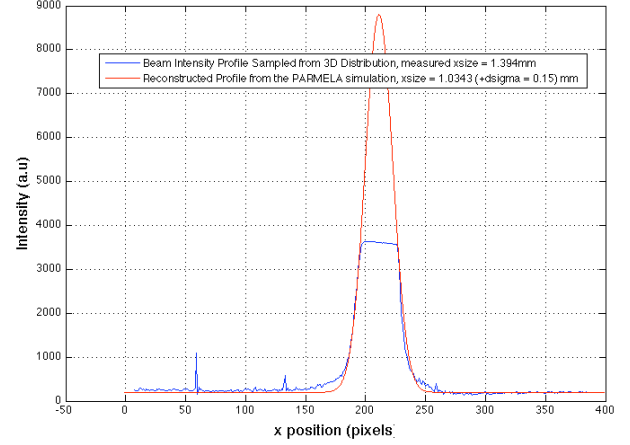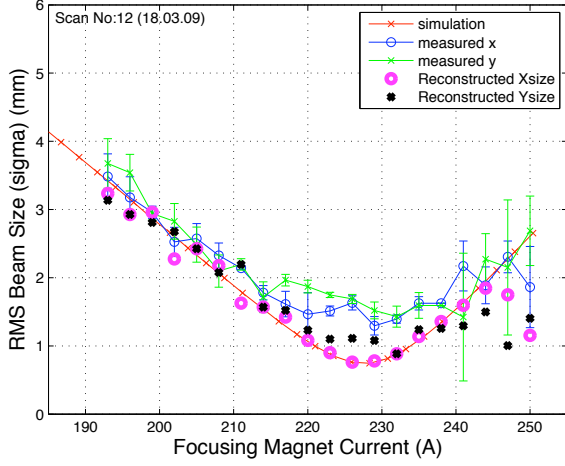Figure 6: The measured and reconstructed beam size scan in comparison with the PARMELA simulation (left).The example of reconstruction for one of the data points (right).
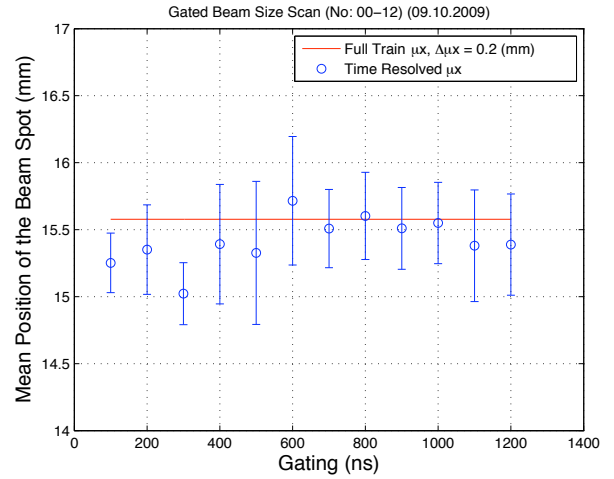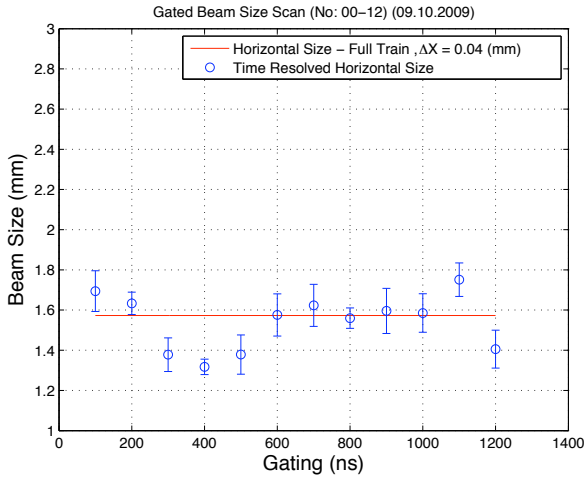

Figure 7: The transverse beam size measurement along the 1.2 μs long train (left). Mean position of the beam spot during the time resolved measurements (right).

train consisted of 1908 bunches at 4.8 MeV under a focusing provided by solenoid current of 200 A. The charge per bunch value was 1.4 nC during the measurement. The red curve denotes the beam size value, measured in a way to capture the image of the full pulse train. For this measurement the camera gate was opened 1.2 μs. The error bars indicate the statistical fluctuations of each point and calculated over a number of subsequent measurements. Δx denotes the statistical error on the full train measurement.

3.2 Emittance Measurement

3.2.1 Multi-Slit Method for Emittance Measurement

The beam emittance has been measured using the multi-slit method. This method is applicable for low energy and space charge dominated beams [17, 18]. The principle of the multi-slit method is to slice the beam transversely into beamlets, therefore the space charge effect becomes negligible during the measurements. The emittance in the slits position can be reconstructed from the beam profile measured after the multi-slits. After a drift section, the momentum distribution can be observed by imaging the beamlets from an OTR screen with a CCD camera. The first and second moments of the beamlets can be obtained from the measured profile, and used for the emittance calculation. For the PHIN set-up an 25 μm thick aluminum OTR screen and an intensified, gated, CCD camera are used.

3.2.2 Data Analysis for Multi-Slit Method

There are two important issues for the analysis of the multi-slit method. The first is the determination of the type and the level of background for the beam profile after the multi-slit mask. The second one is the proper exclusion of the outermost regions in the

tails of the profile, to prevent the misinterpretation of the noise fluctuations as beamlets.

After the slit-mask the beam profile has a background that might be a combination of several effects caused by: the un-stopped electrons by the slit-mask, the overlapping individual beamlets, x-rays or external light pollution and radiation due to heating of the screen. This background has to be determined and subtracted from the profile to be analyzed. FLUKA [19] simulations showed that the mask is able to totally stop a 5.5 MeV electron beam (Figure 8) while 20% of the incoming electrons are back-scattered.
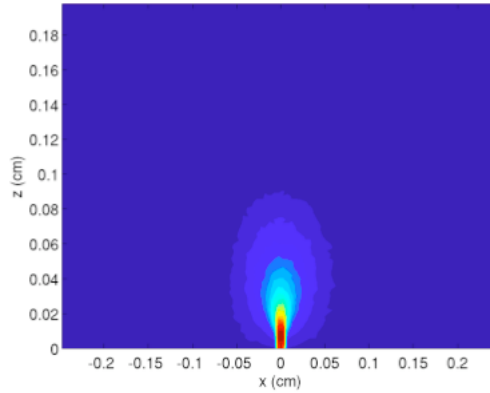

Figure 8: Energy deposition of 5.5 MeV pencil e- beam in a 2 mm thick tungsten slab.

Therefore, under the conditions of current PHIN beam energies and intensities, one can assume that there are no electrons traversing the mask and interacting with the OTR screen except from the ones passing through the slits windows.

Two different models have been assumed for the analysis to describe the background. The first one is a background with a Gaussian shape. The second model assumes the background as a zeroth order polynomial. The analysis have been done for both of the models and the subtraction of a Gaussian background has been found to be more consistent with the simulated data.
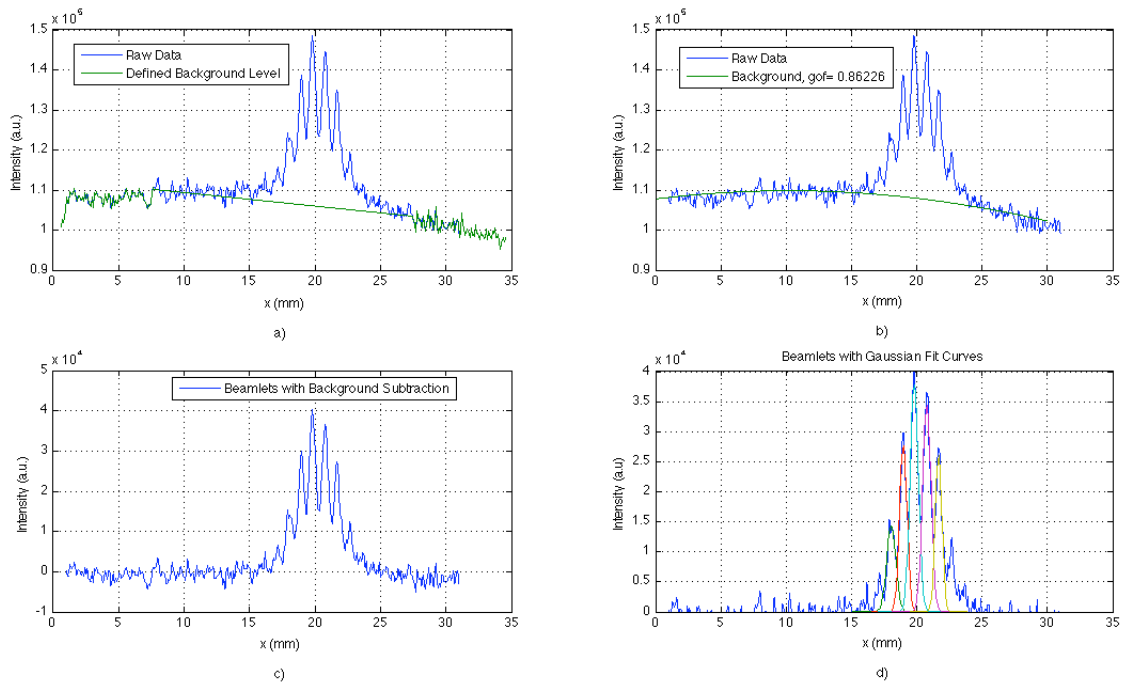
Figure 9: a) The typical beam profile after the multi-slit mask and the region of interest for the background fit. b) Gaussian background on the original profile. c) The beam profile after the Gaussian background subtraction. d) Individual beamlets with the Gaussian fit curves.

The typical beam profile after the multi-slit mask has been shown in Figure 9. In the beginning of the analysis, a region of interest is determined for background fitting, over the raw profile shown in Figure 9-a. The background is determined by fitting the data inside the defined region (Figure 9-b). The initial sigma, mean and the maximum intensity values of the background Gaussian are specified during the fit. Moreover, one can set the initial maximum intensity as variable and define it as *the background subtraction level*. A number of fits can be obtained by varying the background subtraction level and a criteria can be defined to select the most suitable background. The following selection criteria is used: it has been assumed that, after the background subtraction, the

envelope covering the whole beamlets is a Gaussian curve. The quality of fit for the envelope curve could be a measure for the selection of the background subtraction level and the corresponding best defined background.

During the analysis, the background subtraction level has been changed in a range of ± 1200 with the steps of 200, in arbitrary units of intensity, for each profile. The profile after the background subtraction can be seen in Figure 9-c for a particular subtraction level. The first and second moments of each beamlet have been determined for the emittance calculation (Figure 9-d). The *rms* normalized transverse emittance is calculated after the subtraction of each background having different levels. The result of such an investigation is shown in Figure 10. The best fit is determined as the quality of fit (χ^2) value approaches to 1. The subtraction resulting with the best fit of beamlets profile and the envelope has been chosen as the best defined background. The result of the emittance calculation after the subtraction of the this background is 7.4 mm mrad. Analysis result is shown in Figure 11. The emittance for this point has been calculated as 7.9 mm mrad without implementing the background subtraction method described above.
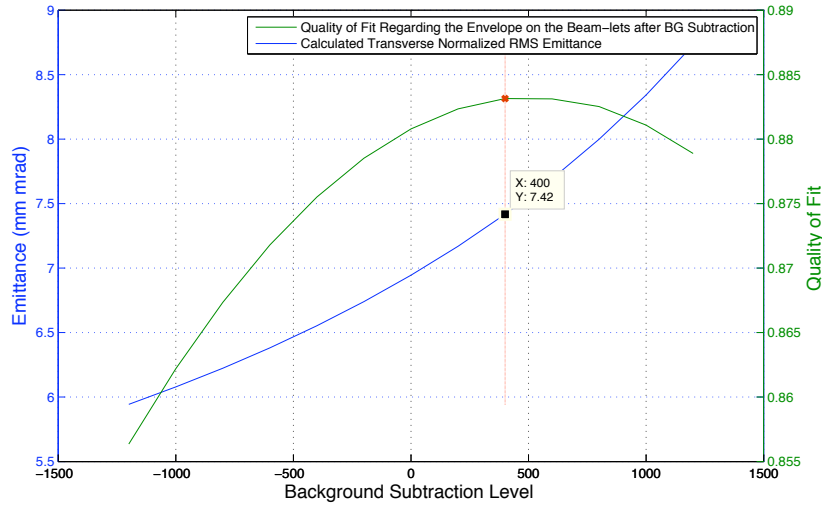

Figure 10: The effect of different background levels on the emittance calculation.

3.2.3 Results

The complete emittance scan has been performed in a wide range of focusing solenoid current, at different laser spot sizes. The emittance scans for the beam with 1.28 nC bunch charge can be seen and compared with the PARMELA simulation in Figure 12. The measurements were performed for laser spot sizes of 3 mm and 4 mm, at energies of 5.2 MeV and 5.5 MeV, respectively. The emittance has been measured for different focusing solenoid settings and each measurement was done with a single-shot OTR imaging. The statistical error has been calculated for each data point regarding these subsequent measurements. It has been shown that the transverse emittance scales with the laser spot size, as expected. The minimum emittance values for the solenoid scans are around 5 mm mrad at 2 mm, 6.5 mm mrad at 3 mm and 12 mm mrad for 4 mm laser spot sizes. The reconstructed phase space for one of the single shot measurements from the emittance scan for 4 mm laser spot can be compared to the PARMELA simulations in Figure 13. The transverse normalized *rms* emittance value is 10.7 mm mrad for this measurements. Although the angle in the phase space is consistent with the simulated one, the measurement is probably not sensitive enough at the tails of the distribution.

Table 3: Systematic error for a single data point on the emittance scan with the values for possible error sources.

	Value
Emittance (mm mrad)	8.2
Slit Width (mm)	0.1
Mask-Screen Distance (mm)	230
Intensity Fluctuations (%)	1.5
$\Delta\varepsilon$ (mm mrad)	1.1
$\Delta\varepsilon(\%)$	13.8

For the systematic error analysis (See Appendix A) a typical error propagation [20] has been done considering parameters of the measurement system included by emittance calculation formula in Eq.1:

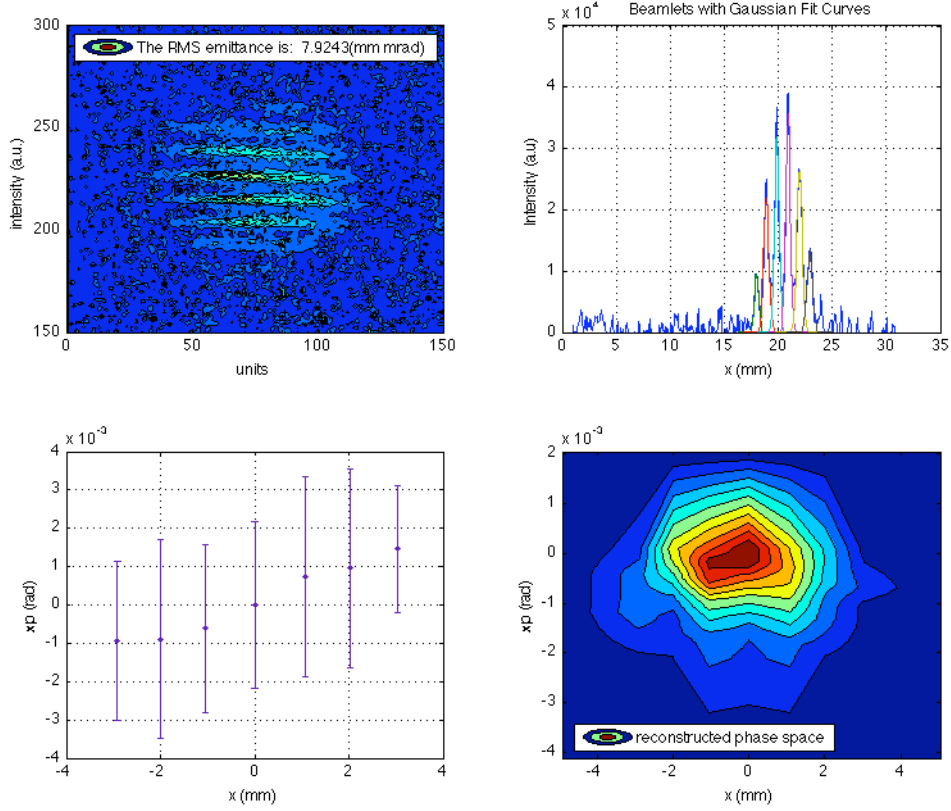$$\varepsilon_{rms} = \sqrt{<x^2><x'^2> - <xx'>^2}. \tag{1}$$

Figure 11: The steps of the emittance analysis. a) The image observed after the multi-slit mask. b) Beam profile with Gaussian fit curves for individual beamlets. c) Mean positions and divergences of each beamlet determined from Gaussian fit curves. d) Reconstructed phase space. The transverse *rms* normalized emittance has been calculated as 7.9 mm mrad for single shot measurement.
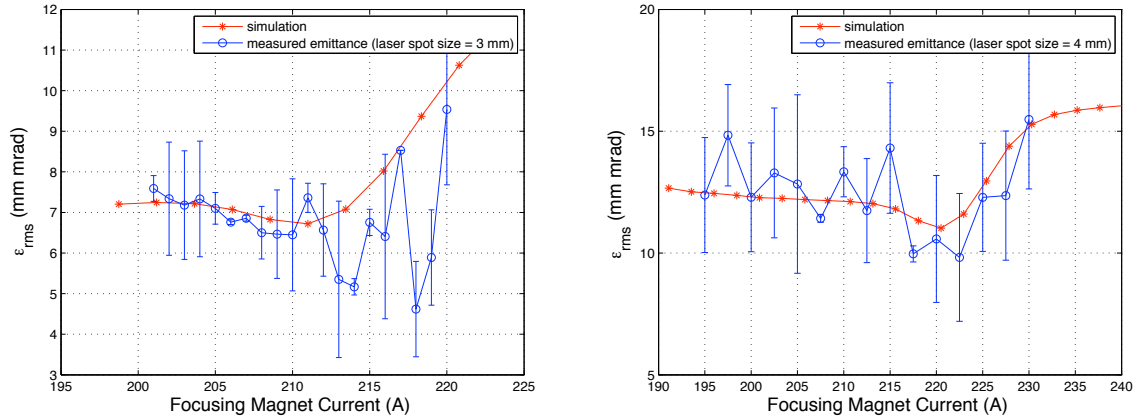

Figure 12: The transverse normalized *rms* emittance vs focusing solenoid current for the 1.28 nC beam for the laser spot sizes of 3 mm (left) and 4 mm (right), at the energies of 5.2 MeV and 5.5 MeV, respectively.

The width of the slits, slit mask to screen distance, and intensity fluctuations of the beam have been considered as the possible error sources in the emittance measurement system. Table 3 summaries the results for a single point from the emittance scan. The scan has been performed with an e^- beam energy of 5.2 MeV, during the data taking the laser spot size was 3 mm. The charge per bunch was 1.28 nC during the measurement. The obtained systematic error for this analysis is 14% which is comparable with the one found due to imperfect background subtraction.

The emittance contributions of the particles in the outermost beamlets and in the beam core can be investigated separately. The results of the analysis for the beam with 1.09 nC/bunch at 5.7 MeV obtained with a 2 mm laser spot size can be found in Figure 14, as a function of focusing current. This figure includes the results of the analysis for the beamlets within the 1σ of the envelope

11
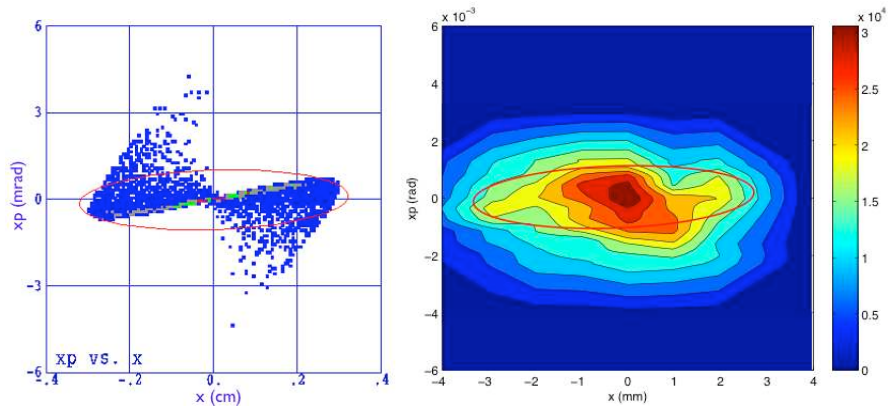
Figure 13: The phase space, simulated (left) and reconstructed from the measurement (right). The emittance was measured as 10.7 mm mrad for 1.28 nC beam at the energy of 5.5 MeV. The measurement was performed with the laser spot size of 4 mm.
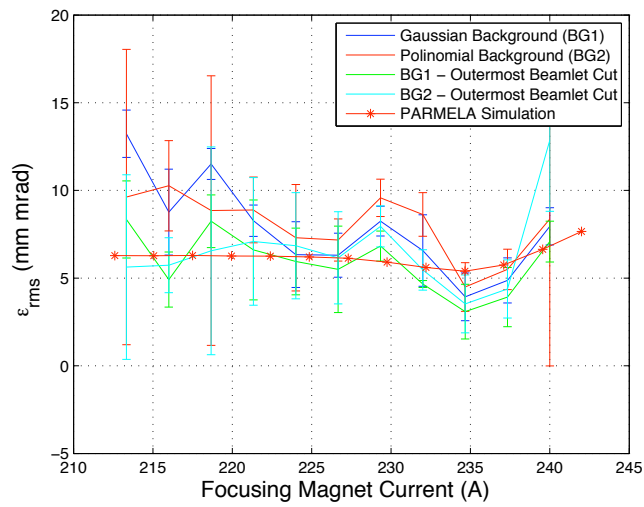
Figure 14: Search for contribution to the emittance from the particles in the outer beamlets.
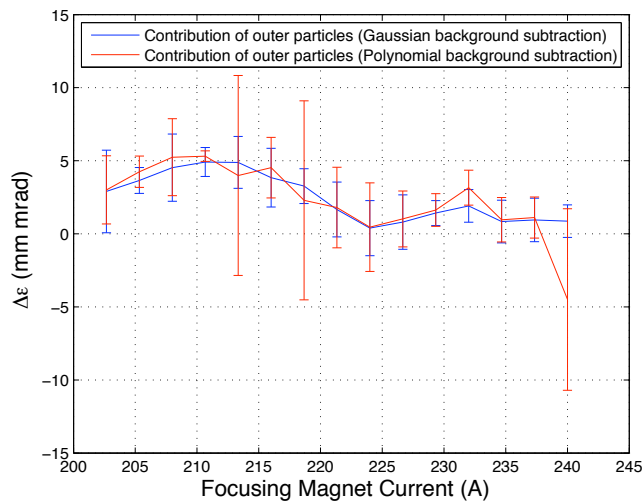
Figure 15: The contribution to the emittance from the particles in the outer beamlets decreases with the increasing focusing.

covering the whole profile. The results after the truncation of the one outer beamlet from both ends have been also shown for the cases where Gaussian and polynomial background models are utilized.

The difference of the calculations when the one outermost beamlet is included and excluded, can give an idea about the emittance

contribution from the outer particles. This contribution is shown in Figure 15 as the difference, explained above, and has been shown to be changing with the focusing solenoid current.

As a result of different approaches, a standard analysis algorithm has been developed for the emittance measurement with multi-slit method. During the analysis the Gaussian background is used. One can assume the background sources as the heating from the OTR screen and the random noise of x-rays generated by the electrons hitting the slit-mask. Therefore the Gaussion model is acceptable as a good approximation. When a polynomial background subtraction is applied, the emittance is measured 8% higher than the result of the Gaussian background, and that can be interpreted as a systematic error. An algorithm has been implemented into the analysis code in order to determine the background subtraction level.

In the tails of the profile the beamlets are indistinguishable from the noise and therefore a beamlet selection cut is applied in these regions. The beamlets occupying the 1σ of the profile are considered as the relevant beamlets for the emittance calculation. The outer particles' contribution to the emittance has been investigated. This contribution changes according to the focusing conditions, as expected.

3.3 Energy Measurement

A time resolved energy measurement of the beam was first attempted using a segmented beam dump, recuperated from CTF2, in March 2009 . The energy spread was not reliably measurable since a fixed Al_2O_3 screen in front of the dump caused electron scattering which lead to a factor of nine widening in the transverse size. The screen was changed to an aluminized Mylar foil[2] in September 2009 to avoid this effect [21]. Regarding the time resolved aspect of the measurement, the goal was to measure the time variation of the energy along the pulse train. To minimize the energy variations during the pulse train, the beam loading has to be compensated. This was obtained by adjusting the timing between the RF and the laser used to extract the electrons. As a result the nearly constant power during the pulse train (indicated with the vertical lines) is shown in Figure 16-a. Figure 16-b shows the current in the dump as function of the beam energy and time that has been successfully measured with the segmented dump, in agreement with the RF.
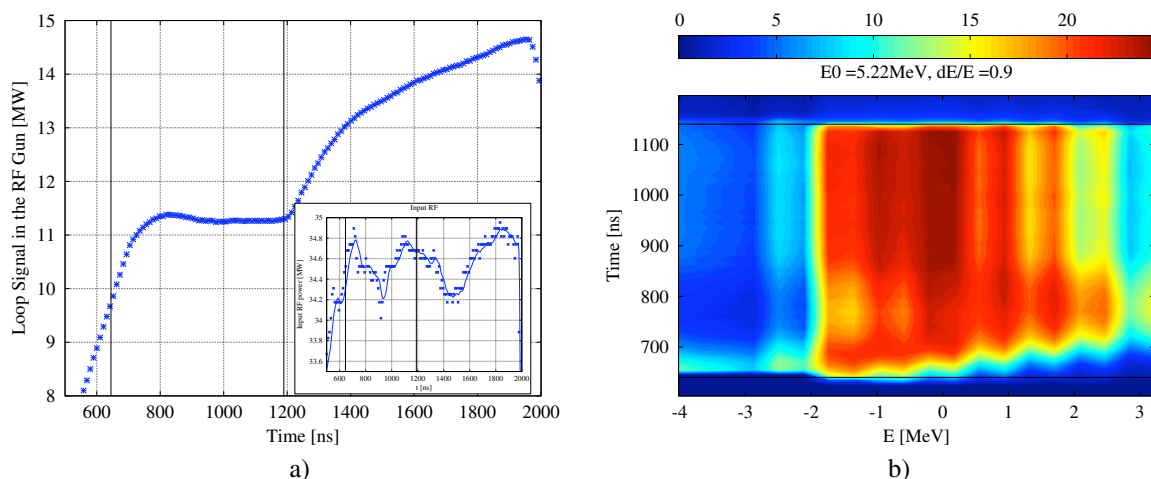

Figure 16: Measurement with beam loading is compensated. (a) RF power in PHIN gun and input power. (b) Segmented dump spectrum.

3.4 Complementary Measurements

The nominal pulse train with a length of 1.2 μs, consisted of 1908 bunches, has been achieved. The beam loading compensation was studied and optimized by adjusting the timing of the beam versus the RF pulse. Figure 17 shows the successful beam loading compensation in the presence of a 1.2 μs long pulse train. In the presence of the beam, a flat top RF pulse has been obtained resulting in a mono-energetic beam. The reflected power is well matched at this point confirming that the input coupler has been adjusted to the correct over-coupling.

For the beam measurements a pulse train with the length of 200 ns has been used. The beam consisted of 300 bunches with a charge of 1.28 nC during the measurements with a laser spot size of 3 and 4 mm at the beam energies of 5.2 and 5.5 MeV, respectively. The measurements with 2 mm laser spot size were done with a charge of 1.09 nC per bunch and at slightly higher energy of 5.7 MeV. The highest achievable charge was 2.53 nC per bunch during the operation, fulfilling the design specification of 2.33 nC for PHIN photo injector.

In Figure 18 the phase scans at different energies have been shown. The particular shape of the curve can be explained by enhanced emission around the on crest phases due to the Schottky effect.

---

[2]Mylar foil has been replaced with an aluminum foil for the upcoming commissioning run in February 2010.
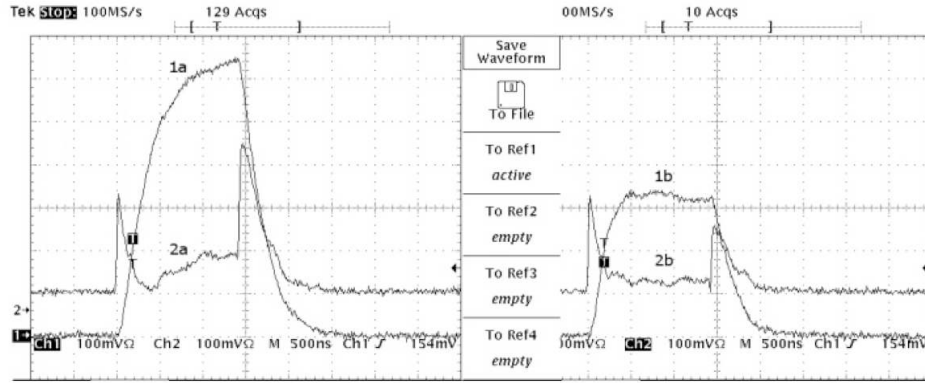
Figure 17: Beam loading. Left: RF power in the gun (1a) and reflected power (2a) when no beam is present. Right: RF power in the gun (1b) and reflected power (2b) when beam is present.
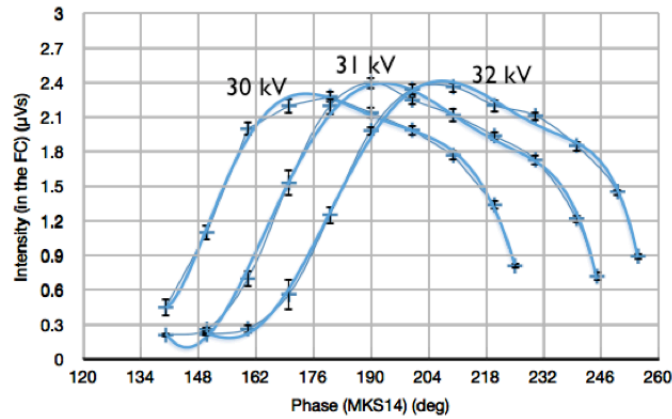

Figure 18: The charge intensity measured in Faraday cup as a function of the klystron phase.

The design specifications have been already achieved for the high charge and the long pulse train. The stability of the beam parameters along the pulse train will be studied in the upcoming run.

4 Conclusion

The beam measurements agreed with the simulations within the measured error ranges. The simulations for the beam size measurements are consistent with the measurements except the focus region. The envelope behavior at the small beam sizes had to be investigated considering the possible limitations from the instrumentation such as CCD saturation effect. Taking into account the saturation effect for the beam profile fitting showed that the beam size scan is consistent with the simulation also around the focus region.

The emittance measurements have been improved with respect to the previous run by replacing the CCD camera with an intensified one enabling the usage of an aluminum OTR screen. The extensive study has been done on the appropriate analysis of emittance measurement with multi-slit method. A standard analysis algorithm has been developed. The Gaussian background has been used for the analysis. The emittance is measured 8% systematically higher than the result of the Gaussian background when a polynomial background subtraction is applied. A correction algorithm has been implemented into the analysis code in order to determine the best defined background. The beamlets occupying the 1σ of the profile is determined as the relevant beamlets for the emittance calculation. The outer particles' contribution to the emittance has been investigated. Under the proper focusing conditions this contribution is found to be minimized.

For the segmented dump, simulations showed that elements in the beamline such as the alumina screen significantly increases the transverse size of the beam, due to multiple scattering and energy loss, to the point this contribution is much larger than the dispersion due to energy spread. Since a reliable energy spread measurement was impossible under this condition, the issue was solved easily in the next commissioning run by replacing the alumina screen with an aluminized Mylar foil.

The focus of the next run will be on the stability measurements along the pulse train. The results will be compared with PARMELA simulations. The optimized beam parameters, deliverable from the photo-injector, will be determined and used as the input for drive beam simulations. The main goal will be to study the current limitations and future modifications in the set-up for the implementation of PHIN photo-injector as the CLIC drive beam electron source.

References

[1] S. Dobert. Integration of the PHIN RF Gun into the CLIC Test Facility. *Prepared for European Particle Accelerator Conference (EPAC 06), Edinburgh, Scotland, 26-30 Jun 2006*.

[2] R. Losito et al. The PHIN Photoinjector for the CTF3 Drive Beam. *Prepared for European Particle Accelerator Conference (EPAC 06), Edinburgh, Scotland, 26-30 Jun 2006*.

[3] G. Geschonke. Results from the CLIC Test Facility CTF3 and Update on the CLIC Design. *EPAC08 Conference Proceedings*, EPAC'08, Genoa, Italy. June 23-27, THYG02, p.2912 (2008). http://www.JACoW.org.

[4] R. Roux. Conception of Photo-injectors for CTF3 Experiment. *International Journal of Modern Physics A, Vol.22, No. 22 (2007) 3925-3941*.

[5] Kwang-Je Kim. RF and Space-Charge Effects in Laser-Driven RF Electron Guns. *Nuclear Instruments and Methods in Physics Research Section A: Accelerators, Spectrometers, Detectors and Associated Equipment*, 275(2):201 – 218, 1989.

[6] B.E. Carlsten. New Photoelectric Injector Design for the Los Alamos National Laboratory XUV FEL Accelerator. *Nuclear Instruments and Methods in Physics Research Section A: Accelerators, Spectrometers, Detectors and Associated Equipment*, 285(1-2):313 – 319, 1989.

[7] A. Barbiero, E. Chevallay, K. Elsener, and R. Losito. Cesium-Telluride Photocathode No. 166. *AB-Note-2007-023 ATB, CARE-Report-07-018-PHIN, CTF3-Note-089*, 2007.

[8] M. Petrarca, V. Fedosseev, and N. Lebas. CTF3 Photo-Injector Laser Amplifier Construction. *CARE-Report-2008-012-PHIN*, CARE-Report-2008-012-PHIN, 2008.

[9] M. Petrarca and et al. CTF3 Photo-Injector Laser. *CLEO/IQEC Proceedings, 2009, Baltimore, Maryland*.

[10] M. Petrarca, K. Elsener, V. Fedosseev, and N. Lebas. CTF3 Photo-Injector: RF Synchronization of the Laser System. *CARE-Report-2008-030-PHIN*.

[11] M. Petrarca, V. Fedosseev, and N. Lebas. CTF3 Photo-Injector Laser System: Conversion to UV. *CARE-Report-2008-019-PHIN*, CARE-Report-2008-019-PHIN, 2008.

[12] M. Petrarca and et al. First Results From the Commissioning of the PHIN Photo-Injector for CTF3. *Particle Accelerators Conference, PAC 09*.

[13] R. Roux, G. Bienvenu, and B. Mercier. Design of a RF Photo-Gun. *CARE Note-2004-034-PHIN*.

[14] R.L. Sheffield and et al. Performance of the High Brightness LINAC for the Advanced Free Electron Laser Initiative at Los Alamos. LA-UR–93-3101; CONF-930855–1.

[15] G. Bienvenu, H. Braun, E. Chevallay, G. Cheymol, M. Divall, S. Doebert, K. Elsener, V. Fedosseev, A. Ghigo, G. Hirst, M. Jore, N. Lebas, R. Losito, B. Mercier, O. Mete, M. Petrarca, C. Prevost, L. Rinolfi(Editor), R. Roux, A. Variola, and C. Vicario. CTF3 3 GHz RF Gun Test at CERN. *CTF3 Note 093*.

[16] L. M. Young and J. Billen. The Particle Tracking Code PARMELA. *Particle Accelerator Conference (PAC 03) 12-16 May 2003, Portland, Oregon*.

[17] Zhang, Min. Emittance Formula for Slits and Pepperpot Measurement. *FERMILAB-TM-1988*.

[18] S. G. Anderson and et al. Space-Charge Effects in High Brightness Electron Beam Emittance Measurements. *Phys. Rev. ST Accel. Beams*, 5(1):014201, Jan 2002.

[19] A. Ferrari, P. R. Sala, A. Fasso, and J. Ranft. FLUKA: A multi-particle transport code (Program version 2005). *CERN-2005-010*.

[20] S. Jolly and et al. Data Acquisition and Error Analysis for Pepperpot Emittance Measurements. *DIPAC09 Conference Proceedings*.

[21] D. Egger, A. Dabrowski, and T. Lefevre. The Status of the Design of the PHIN Spectrometer Line Diagnostics for Time Resolved Energy Measurements and First Results from 2009. *CTF3 Note*.

Part I

Appendix A

For the systematic error analysis a classical error propagation [20] has been done considering parameters of the measurement system included by emittance calculation formula (Eq.2, Eq.3).

$$\varepsilon_{rms} = \sqrt{<x^2><x'^2> - <xx'>^2}$$

(2)

$$= \sqrt{\frac{(\sum_{i=1}^{N} \rho_i x_i^2)(\sum_{j=1}^{N} \rho_j x_j'^2) - (\sum_{i=1}^{N} \rho_i x_i x_i')^2}{(\sum_{i=1}^{N} \rho_i)^2}}$$

(3)

The error on the transverse *rms* emittance can be calculated as the square root of Eq.4,

$$\sigma_\varepsilon^2 = \frac{(\sum_{i=1}^{N} \rho_i^2 x_i^2 \sigma_{x_i}^2 + \frac{x_i^4 \sigma_{\rho_i}^2}{4})(\sum_{j=1}^{N} \rho_j x_j'^2)^2}{\varepsilon^2(\sum_{k=1}^{N} \rho_k)}$$

$$+ \frac{(\sum_{i=1}^{N} \rho_i^2 x_i'^2 \sigma_{x_i'}^2 + \frac{x_i'^4 \sigma_{\rho_i}^2}{4})(\sum_{j=1}^{N} \rho_j x_j^2)}{\varepsilon^2(\sum_{k=1}^{N} \rho_k)}$$

$$+ \frac{(\sum_{i=1}^{N} x_i^2 x_i'^2 \sigma_{\rho_i}^2 + \rho_i^2 x_i'^2 \sigma_{x_i}^2 + \rho_i^2 x_i^2 \sigma_{x_i'}^2)(\sum_{j=1}^{N} \rho_j x_j x_j')^2}{\varepsilon^2(\sum_{k=1}^{N} \rho_k)}$$

$$- \frac{2(\sum_{i=1}^{N} \rho_i^2 x_i^4 x_i'^4 \sigma_{\rho_i}^2 + \rho_i^4 x_i^2 x_i'^4 \sigma_{x_i}^2 + \rho_i^4 x_i^4 x_i'^2 \sigma_{x_i'}^2)}{\varepsilon^2(\sum_{k=1}^{N} \rho_k)}$$

$$+ \frac{\varepsilon^2(\sum_{i=1}^{N} \sigma_{\rho_i}^2)}{(\sum_{k=1}^{N} \rho_k)^2}$$

(4)

where x_i, x_i' are the first and second moments; ρ_i are the relative intensities of the beamlets; σ_{x_i}, $\sigma_{x_{i}'}$, $\sigma_{\rho i}$ are the errors on position, angle and beam intensity fluctuations, respectively.

Part II
Appendix B

The intensity and position stability during the beam size and emittance scans are shown in the figures below.
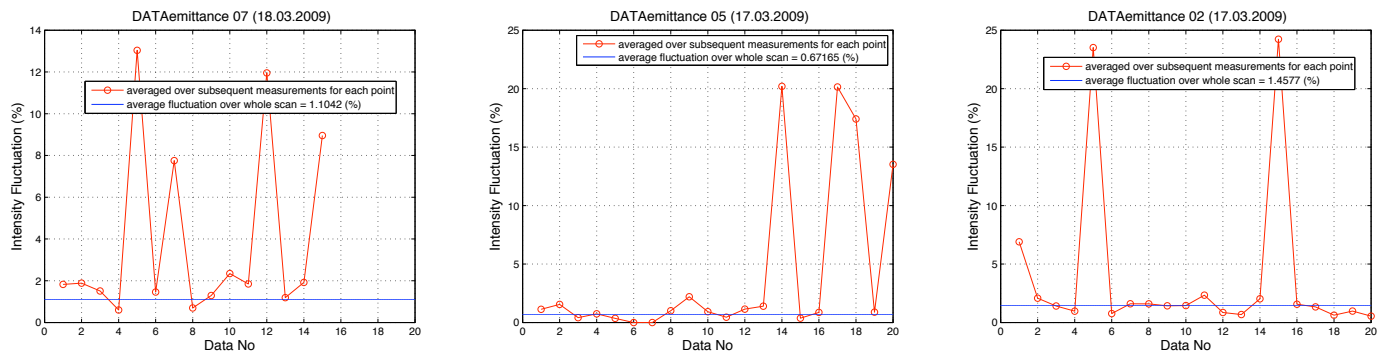

Figure 19: Intensity fluctuations during the emittance scans. Laser spot sizes are 2, 3, 4 mm, respectively.
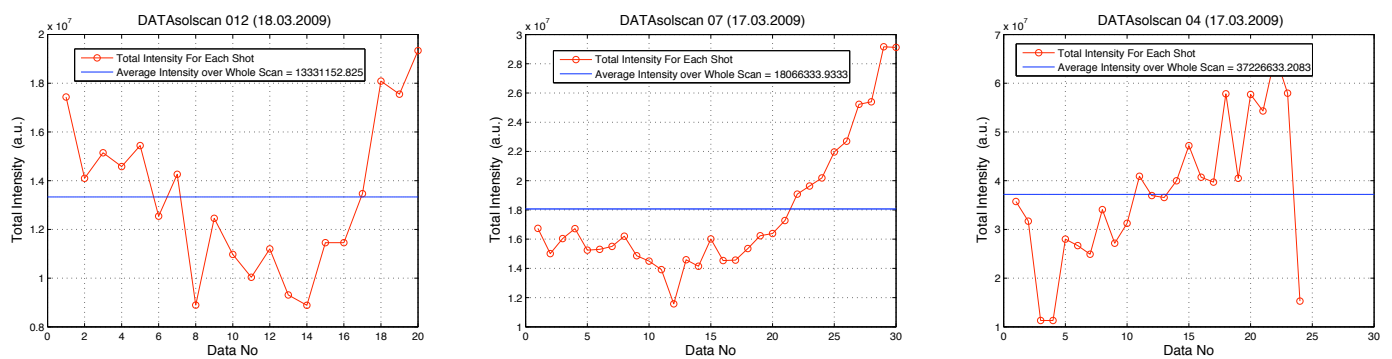

Figure 20: Intensity fluctuations during the e^- beam size scans. Laser spot sizes are 2, 3, 4 mm, respectively.
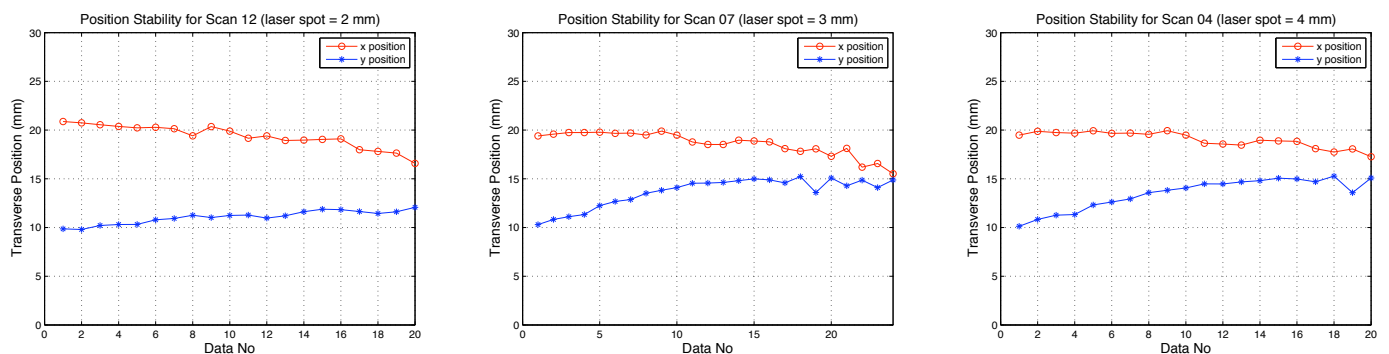

Figure 21: The position stability of the beam spot during the beam size scans.